CrossMark

Effect of folded and crumpled morphologies of graphene oxide platelets on the mechanical performances of polymer nanocomposites

Jin Shang [a, c], Yuli Chen [b], Yanguang Zhou [b], Luqi Liu [a, **], Guorui Wang [a, c], Xianglong Li [a], Jun Kuang [a, d], Qing Liu [a, d], Zhaohe Dai [a, d], Hong Miao [c], Linjie Zhi [a, ***], Zhong Zhang [a, *]

[a] CAS Key Laboratory of Nanosystem and Hierachical Fabrication, National Center for Nanoscience and Technology, Beijing 100190, China
[b] Institute of Solid Mechanics, Beihang University, Beijing 100191, China
[c] Department of Modern Mechanics, University of Science and Technology of China, Hefei 230026, China
[d] University of Chinese Academy of Science, Beijing 100049, China

ABSTRACT

Graphene and its chemical derivate have been taken as promising candidates in composites due to their extraordinary mechanical and physical properties. Different from conventional plate fillers, the embedded graphene fillers exhibit various morphologies (e.g. folded, crumpled, and distorted sheets) inside matrix because of its atomic thickness. In this work, we systematically investigated the influence of graphene oxide (GO) morphologies on the tensile properties of poly(vinyl alcohol)-based nanocomposites at low loading contents. Confocal laser scanning microscopy, as a characterization method, was employed to observe the morphologies of the embedded GO platelets. Tensile mechanical tests and in situ micro-Raman spectroscopy tests indicated that GO sheets with larger aspect ratios exhibited efficient interfacial load transfer and improved mechanical properties at ultra-low filler contents. However, with further increased nanofiller contents, the folded and crumpled GO sheets severely degraded the mechanical reinforcement as induced by interfacial debonding. Molecular dynamic simulation indicated obvious stress concentrations on the wrinkle throughout entire graphene platelet areas. Long-term creep tests confirmed the stress concentration eventually induced the decrease in creep resistance for nanocomposite at a high applied stress levels. All these results aided in understanding the mechanical behaviors of two-dimensional nanofiller-based nanocomposites with huge aspect ratios.

© 2015 Elsevier Ltd. All rights reserved.

1. Introduction

The mechanical reinforcement of conventional composites greatly depends on the load-bearing capability of embedded fillers inside the matrix. Oriented fillers with fairly high aspect ratios are crucial to substantially improving the stiffness of composites. For high aspect ratios, the fiber is sufficiently long for tensile stress to build up until the fiber has a strain equal to that of the matrix and composites. Conversely, for low aspect ratios, stress in the fiber cannot build up to reach a plateau value; thus, the fiber cannot provide very efficient reinforcement because it carries considerably less stress than longer fibers in the same system [1]. Compared with conventional fiber materials, nanofillers such as one-dimensional carbon nanotubes (CNTs), two-dimensional (2D) silicate, and graphene platelets have at least 10^3 aspect ratios, which are conducive to efficient mechanical reinforcement in composites. Our previous works have demonstrated apparent mechanical reinforcement in the modulus, strength, and toughness of CNT-based polymer nanocomposite fibers [2–6]. Similar to the supra reinforcement of CNTs, recently, grapheme becomes a highly promising material for nanocomposites [7–12]. Theoretical calculation based on micromechanical modeling has suggested that randomly oriented graphene platelets with ~10^3 aspect ratio may produce nanocomposites with higher stiffness and strength than randomly

oriented nanotubes [13]. Experimental works have proven that graphene platelets have significantly outperformed CNT fillers in terms of Young's modulus, tensile strength, and fracture toughness in composites [14,15]. However, similar to CNT-filled nanocomposites, the poor dispersion in solvents of graphene and its weak interfacial interactions with polymer matrices greatly limit the widespread use of graphene in composites. Nevertheless, the chemical functionalization of graphene can improve its dispersibility and processability [16–24]. Functional groups bound onto the surface of graphene oxide (GO) sheets can improve interfacial bonding between GO and matrix, as observed for functionalized CNT-based nanocomposites [2,25–27]. Thus, various GO-incorporated water-soluble polymer nanocomposites have been prepared, and apparent mechanical reinforcement has been achieved [27–31]. For instance, Xu et al. [27] found that the Young's modulus and tensile yield strength of composites containing 3 wt.% GO could reach up to 4.8 GPa and 110 ± 7 MPa respectively, indicating 128% and 65% improvement compared with pure matrix. Zhao et al. investigated the influence of GO filler content on the tensile mechanical properties of nanocomposites, and the increasing trend was less obvious at high loading contents because of the inevitable stacking of GO sheets [28]. Coleman et al. compared the difference in reinforcement for graphene-based composites with ~1000 and ~2000 aspect ratios [29]. They predicted that reinforcement would approach theoretical limit once graphene platelets (aspect ratio $\approx 10^4$) become available. However, most works have focused on static mechanical improvement, and only a few have paid attention to the creep of graphene and its chemical derivate-based nanocomposites [30,31].

Both experimental studies and atomic simulation [32,33] have confirmed the presence of ripples, wrinkles, and corrugation in graphene sheets resulting from thermal fluctuations, structure defects, and surface functionalization [33–35]. The presence of wrinkles in sheets also greatly affects many intriguing physical properties of graphene, such as thermal conductivity, carrier mobility, and wettability [36–38]. Reports on the influence of wrinkled and crumpled morphologies of graphene platelets on the mechanical performance of nanocomposites are limited [39,40]. As expected, the wrinkled nature of graphene sheets provides less than the optimal reinforcement because of their straightening deformation mode rather than stretching between C–C bonds under in-plane tensile stress. However, the influences of crumpled, wrinkled and folded graphene sheets on mechanical behaviors and deformation modes have not yet been experimentally demonstrated. The underlying mechanism has also not been completely understood yet.

In the present work, GO sheets with aspect ratios of ~1.5 × 10³ and ~7.4 × 10⁴ were used to prepare GO/poly(vinyl alcohol) (PVA) nanocomposites through solution-casting method. We systematically compare the mechanical properties of nanocomposites with different aspect ratios at relatively low contents (<1 wt.%). Confocal laser scanning microscopy characterization indicated the crumpled and irregularly folded microstructural features of GO sheets inside the matrix. Both static tensile and in situ micro-Raman spectroscopy tests were used to evaluate the reinforcement of GO platelets at macroscopic and microscopic levels. The influences of crumpled and folded GO sheets on the mechanical performance of composites were determined by experiment and molecular dynamic (MD) simulation. The influence of wrinkled, folded, and distorted morphologies of GO sheets on the mechanical performances of nanocomposites were examined through long-term tensile creep tests based on the time–temperature superposition principle (TTSP). Our work can help elucidate the mechanical behaviors of 2D filler-reinforced polymer nanocomposites, particularly those with huge aspect ratios.

2. Experimental

2.1. Material

Preparation of small-size GO sheets (s-GO): s-GO was prepared from purified natural graphite (obtained from Qingdao Yingshida graphite Co., Ltd., with an average size of 20 μm) by a modified Hummers method [41]. Under agitation, graphite powder (4 g) and NaNO₃ (3 g) were mixed with H₂SO₄ (250 ml, 98 wt. %) in an ice bath, and KMnO₄ (25 g) was slowly added to prevent the temperature from exceeding 20 °C. The reaction was kept at 20–30 °C for 2 h with gas release, and then deionized water was gradually added. The resultant bright-yellow suspension was diluted and further treated with a H₂O₂ solution (30%), followed by centrifugation and careful washing to clean out remnant salt. Colloidal dispersions of individual GO sheets in water (5 mg/ml) were prepared with the aid of an ultrasonic bath.

Preparation of large-size GO sheets (l-GO): The detailed experimental procedure for the preparation of l-GO sheets is described as follows [42]. Natural flake graphite (2 g) with an average size of 500–600 μm, NaNO₃ (2 g), and concentrated H₂SO₄ (96 ml) were mixed at 0 °C. Then, KMnO₄ (12 g) was gradually added to the mixed solution while keeping the temperature at 0 °C. The mixture obtained was stirred at 0 °C for 90 min, and then at 35 °C for 2 h. Deionized water was slowly dropped into the resulting solution, over a period of around 30 min, to dilute the mixture. Then deionized water (200 ml) was added followed by H₂O₂ (10 ml, 30%), and the stirring continued for 10 min to obtain a graphite oxide suspension. The graphite oxide deposit was collected from the graphite oxide suspension by high-speed centrifugation at 12,000 rpm for 40 min, and repeatedly washed with deionized water until pH = 7. Then a mild sonication (40 W, 15 min) was used to exfoliate the graphite oxide to obtain a GO suspension. To obtain uniform l-GO sheets, a low-speed centrifugation at 3000 rpm was first used to remove thick multilayer sheets until all the visible particles were removed (3–5 min). Then the supernatant was further centrifuged at 5000 rpm for 5 min to separate large sheets (precipitate) and small sheets (supernatant). Finally, the obtained precipitates containing large sheets were re-dispersed in water to get l-GO sheet suspension (5 mg/ml).

The average aspect ratio of individual GO sheets was obtained by $A_f = \ell/t$, where ℓ presents half of the perimeter of individual GO sheets, t is average thickness of individual GO sheet referred Ruoff's work [43]. More than 100 individual GO sheets based on SEM images were analyzed for s-GO and l-GO sheets respectively.

Preparation of GO/PVA composites: PVA with Mw $\approx$ 120 000 was purchased from Beijing Chem. Reagents Co. (Beijing, China) and used as received. The procedures for preparing PVA/GO composite films are described as following: PVA (8 g) was dissolved in 392 ml deionized water at 90 °C to give a 2 wt. % solution. Then, PVA (25 ml) solution was added to 0.1, 0.5, and 1 ml GO dispersion (5 mg/ml), and the mixtures were well stirred immediately to obtain uniform dispersions. The solution was further cast on the Petri dish dried overnight under vacuum at 60 °C. The weight contents of GO in the three films described above were calculated to be about 0.1, 0.5 and 1 wt. %, respectively. The filler concentration was transformed from mass fraction (wt. %) to volume fraction (vol. %) by the following Equation (1):

$$v = \frac{w\rho_p}{w\rho_p + (1-w)\rho_g} \tag{1}$$

where, v and w are the volume fraction and mass fraction of GO sheets. ρ_p and ρ_g represent the density of PVA matrix and GO sheets, which can be taken as 1.3 g/cm³ and 2.2 g/cm3 [44,45], respectively.

The volume fractions of GO sheets inside PVA matrix can be obtained as 0.06, 0.3, and 0.6 vol. %. Samples of GO/PVA composites prepared in this manner were cut by a razor blade into strips (30 mm × 2 mm) and then dried at 60 °C for 12 h with a vacuum oven before mechanical tests.

2.2. Characterization

Typical tapping-mode Atomic force microscopy (AFM) measurements were performed using Dimension Icon (Nanoscope IIIa SPM system, Bruker Nano, USA). Samples for AFM characterization were prepared by depositing a dilute GO solution onto a freshly cleaved mica surface and allowing it to dry in air. The dispersion state of GO sheets was studied by scanning electron microscopy (SEM) (HITAHI S-4800). The morphology of GO sheets inside PVA matrix was observed by Research Inverted system Microscope IX81 (Olympus, Japan), CCD: DP71 Olympus, with a laser of 633 nm.

2.3. Mechanical test

A dynamic mechanical analyzer (TA, DMA Q800) was employed to evaluate the mechanical properties of GO/PVA nanocomposites. The stress–strain tests were conducted in displacement ramp mode with a pre-strain 0.01% and a ramp rate of 300 μm/min. The time–temperature superposition principle (TTSP) was adopted for short-term creep tests of GO/PVA nanocomposites performed at different temperature levels. The temperature range was in the range of 35–60 °C with 5 °C interval, and the isothermal tests were run on the same specimen in the temperature range. The creep stress was applied for 10 min at each temperature. Prior to the measurement for each test, the specimen was equilibrated for 5 min at each temperature, in order to evenly adjust for the correct temperature of the sample.

2.4. Molecular dynamics (MD) simulations

The MD simulations are performed by the large-scale atomic molecular massively parallel simulator (LAMMPS) [46]. The SiO$_2$substrate is considered as a rigid body. The adaptive intermolecular reactive empirical bond order (AIREBO) is taken to describe interactions between carbon atoms of the graphene [47]. The cutoff parameter is taken as 0.192 nm for REBO potenti [48] In order to simulate the interactions between the graphene and the substrate, the Lennard-Jones (LJ) potential with parameters $\sigma = 0.2935$ nm and $\varepsilon = 0.00513$ eV is employed [49]. Constant temperature MD simulations are carried out at 5 K with NVT ensemble. The equations of motion are integrated using the Verlet leapfrog method with a time step of 2 fs.

3. Results and discussion

The Halpin–Tsai equation is widely used to predict the modulus of unidirectional or randomly distributed filler-reinforced composites [26,28,50]. Fig. S1 shows composite moduli initially increase with increased filler aspect ratio, but this trend eventually becomes negligible. In the current work, we used two types of GO sheets with different aspect ratios, namely, *s*-GO sheets with an average aspect ratio ~1.5 × 10³ and *l*-GO sheets with an average aspect ratio ~7.4 × 10⁴. Fig. 1a and b presents the typical SEM images of GO sheets with different size distributions. Quantitative evaluation of such difference is discussed later. Compared with *s*-GO sheets that have relatively flat, smooth morphology, *l*-GO sheets exhibit folded morphology (circle in Fig. 1b). AFM characterization (Fig. 1c and d) offers straight forward evidence for exfoliated individual GO sheets, in which the thickness of GO sheets is within a range of 0.8–1.2 nm, as indicated by the contour curve in Fig. 1e and f.

The area distributions of the as-prepared GO sheets were determined by plotting the area distribution histogram based on 100 individual GO sheets (Fig. 2a and b). A difference of almost three orders of magnitude is observed between the mean sheet areas of *s*-GO and *l*-GO sheets (Table 1). Specifically, >70% of individual GO sheets are located in the area of 0.4–0.7 μm² for *s*-GO samples, whereas 70% of individual sheets are located within the area of 750–1750 μm² for *l*-GO samples. A statistical method based on the two-parameter Weibull model [51] was adopted to evaluate
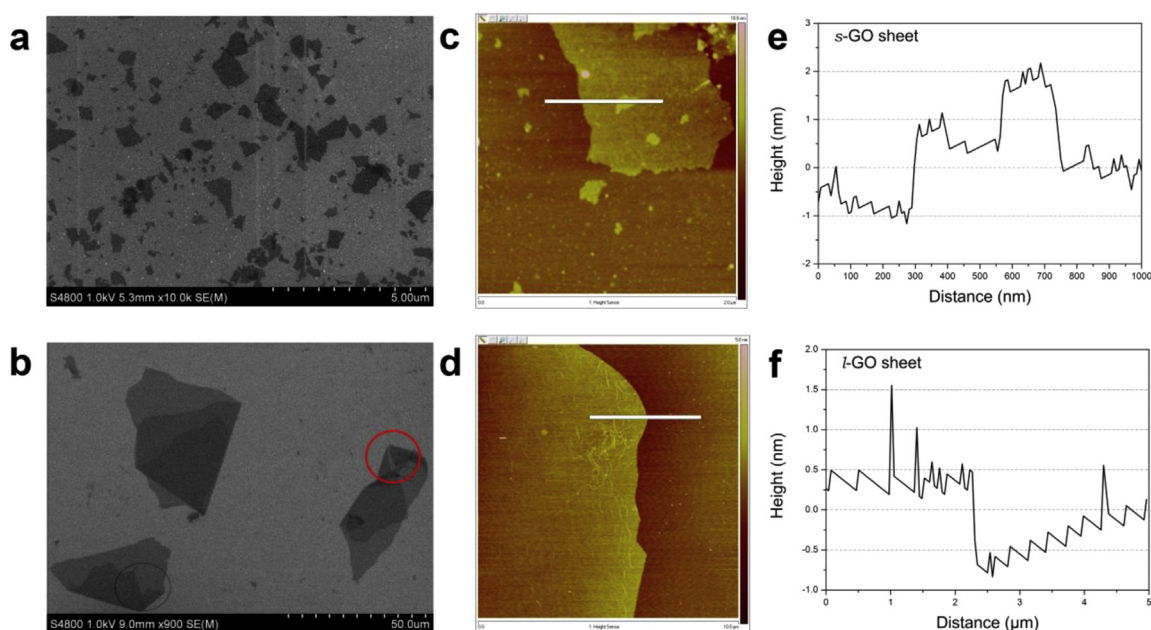
Fig. 1. (a, b) Typical SEM images of GO sheets with different lateral dimensions; the folded morphology of *l*-GO sheets is circled in 1b. (c, d) AFM images of GO sheets. (e, f) Height profiles of individual GO sheets along the solid lines shown in Figures 1c and 1d.
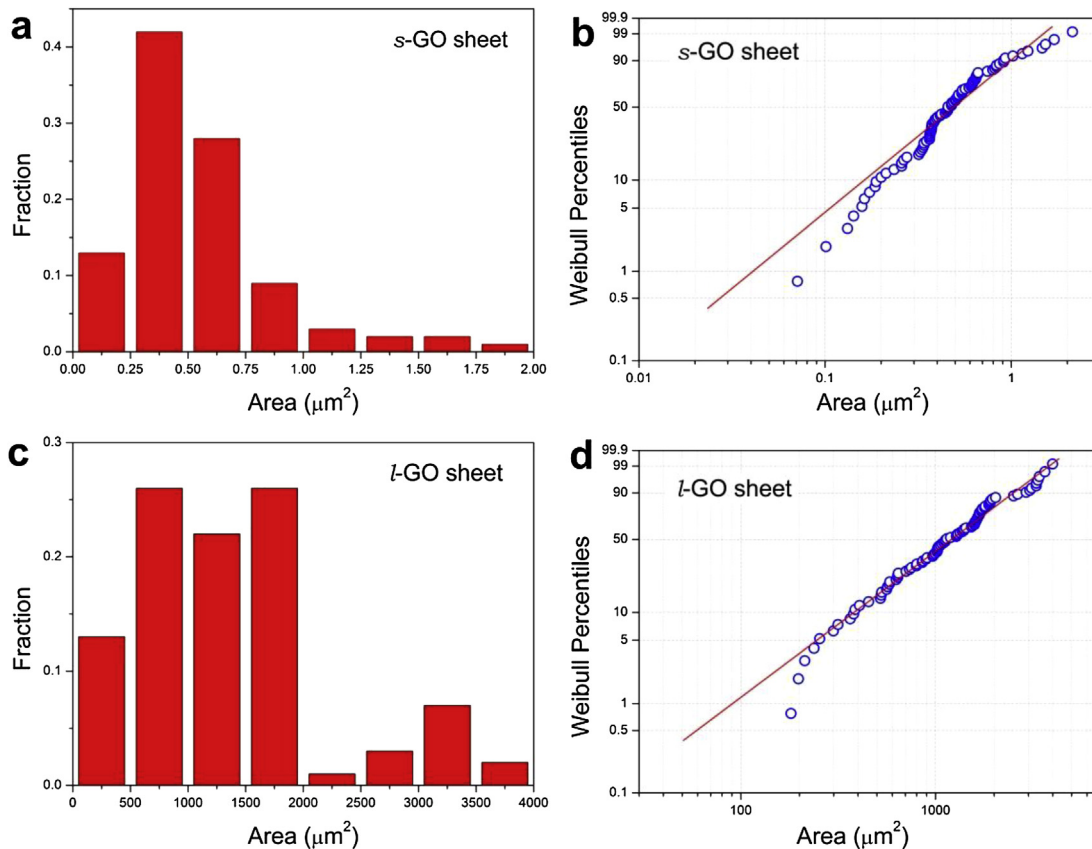
Fig. 2. Area distributions of s-GO sheets (a) and l-GO sheets (c) based on 100 individual sheets for each specimen; Weibull plots of area distributions of s-GO sheets (b) and l-GO sheets (d).

the area distributions of GO sheets using the following equation (Equation (2)):

$$F(x) = 1 - e^{-\left(\frac{x}{\beta}\right)^{\alpha}} \tag{2}$$

where x is the measured areas of GO sheets, F is the cumulative probability of x, α is the shape parameter, and β is the characteristic area at the cumulative probability of 63.2%. Table 1 summarizes the relevant Weibull parameters derived from Fig. 2c and d. The shape parameter (α) values of s-GO and l-GO are 1.71 and 1.64, respectively, and this minor difference indicates similar distributions of sheet areas. Meanwhile, the scale parameter (β) values of 0.61 and 1506 μm^2 for s-GO and l-GO samples, respectively, indicate the characteristic areas of GO sheets. For individual l-GO sheets with folded morphology, the contribution of the folded area and perimeter to the total area and perimeter were also considered. The derived aspect ratios of s-GO and l-GO sheets are ~1.5 × 10³ and ~7.4 × 10⁴, respectively. Compared with previously reported GO sheets having lateral dimensions of a few micrometers [26–28], our l-GO sheets with such a giant size have not yet been utilized in nanocomposites.

Fluorescence quenching microscopy (FQM) [52] and transmission electron microscopy (TEM) are widely used to characterize the size, agglomeration, and restacking of graphene and its chemical derivate sheets [43,49,53–55]. Unlike the tedious sample preparation procedures required by FQM and TEM, an easy and simple method based on confocal laser scanning microscopy was performed to characterize the corrugation and folded microstructural features of embedded l-GO sheets inside matrix. Fig. 3a and b shows the various morphologies of embedded GO sheets with different lateral dimensions. The l-GO sheets with giant lateral dimensions (approximately ≥ 20 μm) evidently show folded and crumpled morphologies. Some l-GO sheets even exhibit twisted and distorted morphologies (Supporting information Fig. S2). Conversely, embedded s-GO sheets exhibit relatively flat morphology inside the polymer matrix.

As aforementioned, the mechanical performance of GO-based nanocomposites is significantly affected by the sheet aspect ratios. In our previous work, we have demonstrated that H-bonding between oxygen-containing groups (e.g., hydroxyl, carboxyl, and epoxide) of GO sheets and hydroxyl groups of PVA polymer chains enable efficient load transfer [56]. Fig. 4a and b presents the typical stress−strain curves of s-GO/PVA and l-GO/PVA nanocomposites with different volume fractions. With increased filler volume fractions, the tensile modulus and strength of all GO/PVA nanocomposites apparently improve. Compared with s-GO/PVA nanocomposites, l-GO/PVA nanocomposites show more obvious

Table 1
Weibull parameters determined from the area distributions of GO sheets and aspect ratio of GO sheets.

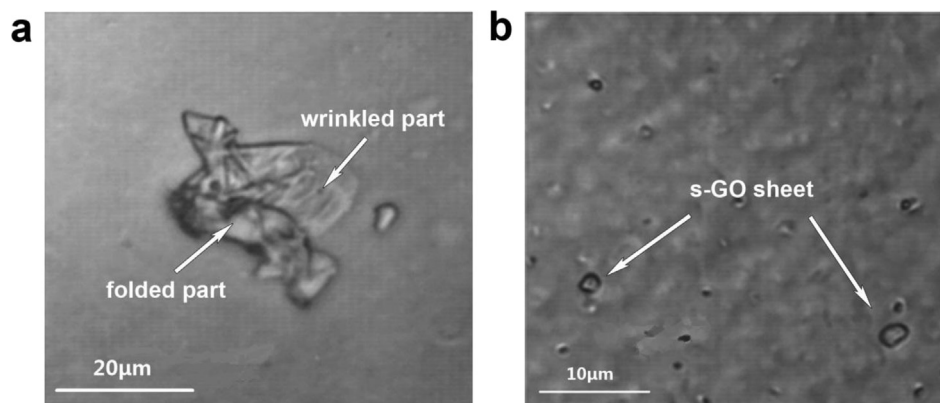| GO sheets	Shape parameter, α	Scale parameter, β (μm^2)	Area (μm^2)	Perimeter (μm)	Aspect ratio
s-GO	1.71	0.61	0.54 ± 0.34	3.00 ± 0.94	1.5 × 10³
l-GO	1.64	1506	1342 ± 868	148 ± 59	7.4 × 10⁴

Fig. 3. Images of *l*-GO (a) and *s*-GO (b) sheets for 0.3 vol.% GO/PVA nanocomposites characterized by confocal laser scanning microscopy.

mechanical enhancement at lower filler contents. For instance, the modulus and strength of *s*-GO/PVA nanocomposites with 0.3 vol.% GO are 3.47 GPa and 80.00 MPa, whereas those of *l*-GO/PVA nanocomposites also with 0.3 vol.% GO are 3.92 GPa and 97.50 MPa, respectively (Fig. 4c and d). Compared with *s*-GO/PVA nano-composites, *l*-GO/PVA nanocomposites with a large aspect ratio (~7.4 × 10^4 vs. ~1.5 × 10^3) exhibit better interfacial stress-transfer efficiency under loading condition, which eventually leads to better mechanical reinforcement. Micromechanical analysis based on in situ Raman spectroscopy provides more detailed information, and will be discussed later. With further increasing filler content up to 0.6 vol.%, both modulus and strength for *l*-GO/PVA nano-composites show negligibly changes. Moreover, the elongation at break for GO/PVA nanocomposites shows gradually decreases with increasing GO loading, and the decreased trend is more apparent for *l*-GO/PVA nanocomposites. The embedded *l*-GO sheets with

wrinkled and folded conformations as shown in Fig. 3a and S2 easily form local stress concentration when subjected to external deformation, and then lead to the occurrence of interfacial debonding especially at high stress level. Consequently, for *l*-GO/PVA nanocomposite having high filler content, the occurrence of local interfacial debonding in response to external stress would accelerate the initiation and propagation of cracks, and eventually result in lower failure strain [28].

Interfacial stress transfer from matrix to GO sheets in GO/PVA nanocomposites and possible deformation modes were examined by in situ micro-Raman spectroscopy based on our previous work [57]. Fig. 5a shows the typical Raman G band of GO sheets in nanocomposites. Compared with that of graphene sheets, the asymmetrical broadening of the G band profile of GO sheets can be ascribed to defects (the D′ band at ~1620 cm^{-1}) and to the sym-metry breaking of the conjugated π systems of GO sheets arising
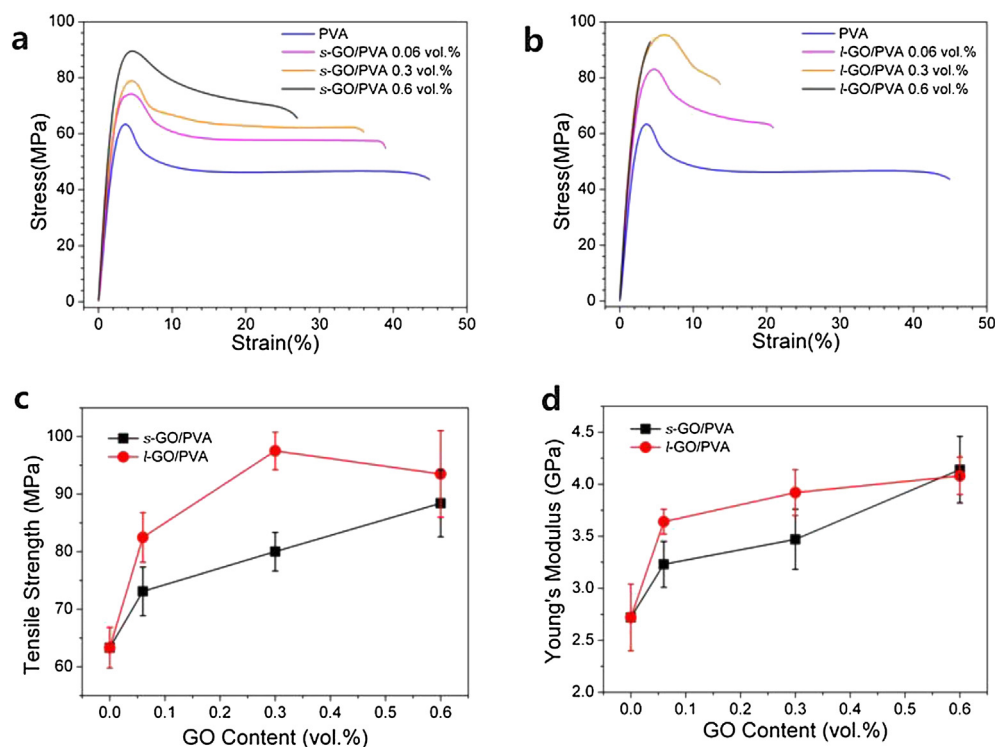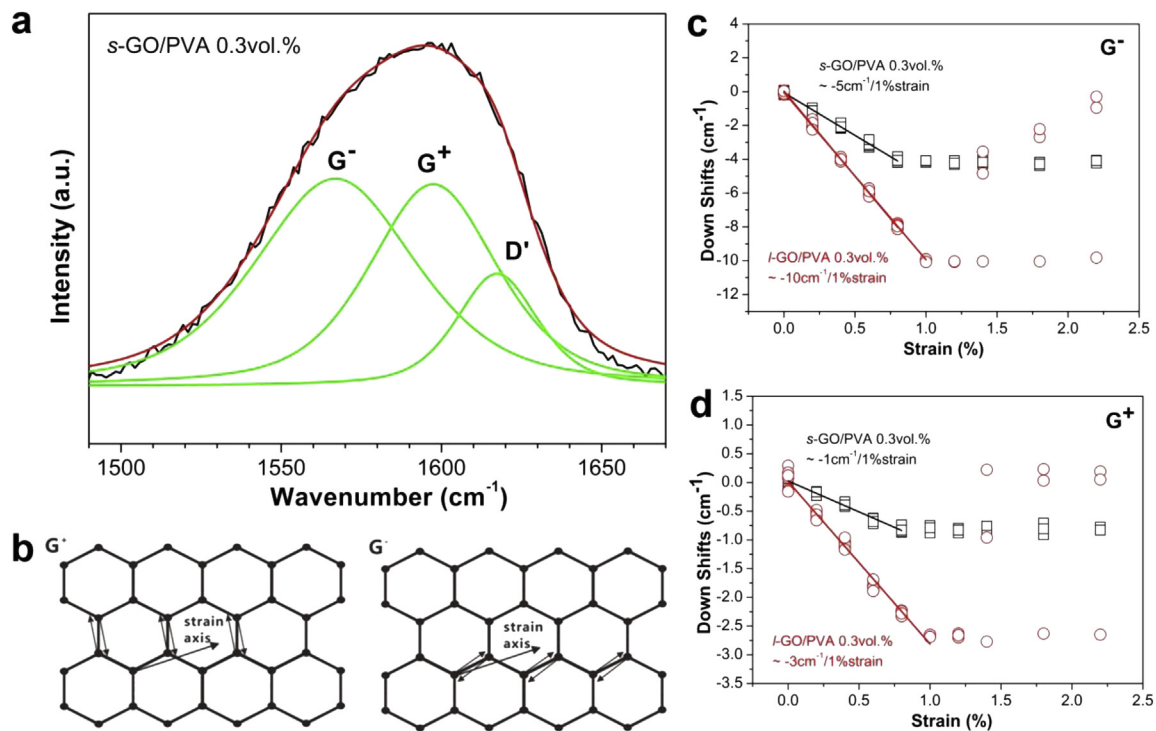

Fig. 4. (a, b) Representative stress–strain curves of GO/PVA nanocomposites with different GO loadings. (c) Tensile strength; and (d) Young's modulus of GO/PVA nanocomposites vs. various GO loadings.

Fig. 5. (a) Typical G band of 0.3 vol.% GO/PVA nanocomposites well fitted with three peaks of G−, G+, and D′; (b) eigenvectors of G− and G+ bands that are perpendicular to each other, with the G-band polarized along the strain axis; Raman shifts of the G− (c) and G+ (d)bands of *l*-GO and *s*-GO in nanocomposites as a function of applied strain.

from the introduced various functional groups [57]. Herein, the Raman G band of GO sheets is well fitted with the three peaks of G−, G+, and D′. Fig. 5c and d summarize the various trends of the G− and G+ peak positions as a function of applied strain for both *l*- and *s*-GO/PVA nanocomposites. The downshifted trend of GO/PVA nanocomposites is found to have the following two-stage features: linearly decreased region at low strain level and plateau region at high strain level. The downshift trends of G+ band are less obvious than that of G-band for GO/PVA nanocomposites, consistent with our previous results [57]. As discussed by Mohiuddin et al. [58], the different shift trends of G− and G+ bands are mainly determined by their eigenvector orientations, in which G-band is polarized along the strain axis and G+ band is perpendicular to it (Fig. 5b). The elongated carbon−carbon bond distance is more apparent in the direction along the strain axis and thus becomes more sensitive to applied loads. Furthermore, the downshift rates of G-band can reflect the local load-bearing capabilities of GO sheets in polymer during tensile deformation. We can infer from Fig. 5c that in the linearly down-shifted region (at low strain level), the load-bearing capability of *l*-GO sheets is visibly stronger than that of *s*-GO sheets. Specifically, the G band shift rate is ~5.0 cm−1 per 1% strain for *s*-GO/PVA nanocomposite samples, whereas the shifted rate is ~10.0 cm−1 per 1% strain for *l*-GO/PVA nanocomposite. Notably, the turning point of strain as an end of the linear region for *l*-GO/PVA nanocomposite (~1.0%) is slightly higher than that of *s*-GO/PVA nanocomposite (~0.8%). In conventional short fiber-reinforced composites, the fiber length is suggested to be at least 10 times larger than the critical length of fiber to obtain good reinforcement [1]. In our work, the lateral dimensions of *s*-GO sheets are in a few micrometers, which is close to the critical length of an individual graphene sheet (~3 μm), as reported by Gong et al. [59] Expectedly, according to shear-lag model [1], the strain that *s*-GO sheets carried cannot reach matrix strain when subjected to tensile stress. In comparison, the *l*-GO sheets with around 20 μm width would

enable the strain that *l*-GO sheets carried to be equal to matrix strain at low strain level. The larger shift rate of G band for *l*-GO sheets in comparison with that of *s*-GO sheets further confirms our analysis. Fig. S3 shows that the G− and G+ band peak position of 0.3 vol.% GO/PVA nanocomposites linearly shift as a function of applied strain up to 0.8%. Apparently, for *l*- and *s*-GO/PVA nanocomposites, the G band shift along the unloading trace well coincides with that of the loading one, further indicating the reversible tensile deformation of nanocomposites in low strain region. Subsequently, above a certain strain value, Raman G band reaches a plateau due to interfacial sliding in nanocomposites. Meanwhile, Fig. 5c shows that some G bands of *l*-GO/PVA nanocomposites recover to the unstrained state, further indicating the occurrence of interfacial debonding. Combined with the optical
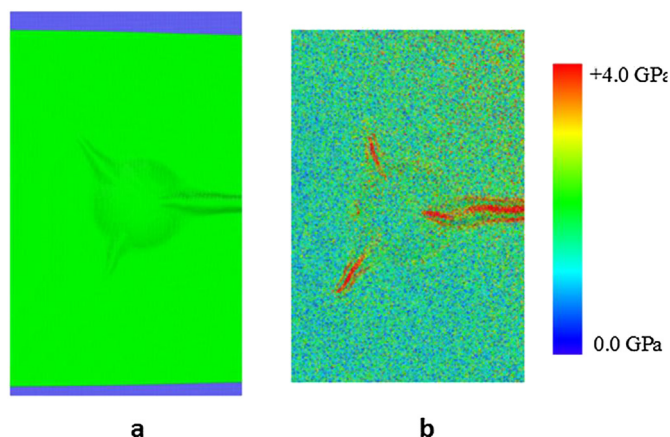
Fig. 6. Wrinkled morphology (a) and corresponding von Mises stress distribution (b) of a monolayer graphene deposited onto a rigid substrate.
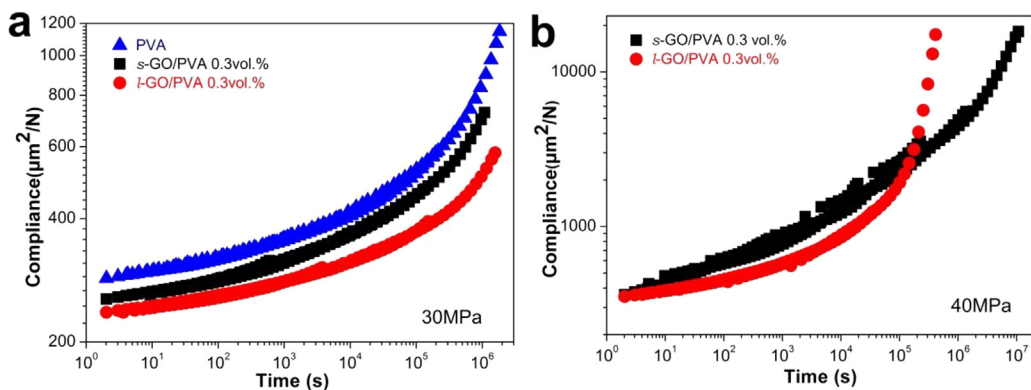
Fig. 7. Master curves of GO/PVA nanocomposites presented as creep compliance at different stress levels: (a) 30 and (b) 40 MPa.

images shown in Fig. 3a and b, we conjecture that the folded and crumpled morphologies of *l*-GO sheets induce interfacial debonding at large strain levels. The non-uniform stress distribution within the folded and crumpled GO sheets would easily induce the local stress concentration, and then lead to the interfacial debonding in composites at large strain level.

To confirm the non-uniformity of stress distribution within a wrinkled GO platelet, we used MD simulation to analyze the stress state of an individual graphene sheet. Fig. 6a shows a monolayer graphene with wrinkled morphology deposited onto a rigid substrate. Von Mises stress distribution analysis indicates that the stress is not uniformly distributed around the whole graphene area. Instead, obvious stress concentrations were observed around the wrinkles (Fig. 6b). Thus, we inferred that the embedded *l*-GO sheets with folded and crumpled morphologies would easily induce the interfacial debonding because of the non-uniform stress distribution.

The influences of the folded and crumpled morphologies of embedded GO sheets on the mechanical performance of nanocomposites, particularly time-related properties, are investigated by long-term creep properties based on TTSP [60,61]. The relation between temperature and shift factor can be generally described by the Arrhenius Equation [62,63].

$$\ln a_T = \frac{E}{R}\left(\frac{1}{T} - \frac{1}{T_0}\right) \tag{3}$$

where a_T is the horizontal shift factor, R is the universal gas constant, E is the activation energy, T_0 is the reference temperature, and T is the experimental temperature. The master curves in terms of creep compliance for *s*- and *l*-GO/PVA composites with 0.3 vol.% GO at different stress levels are presented in Fig. 7. Based on these curves, we can predict the long-term property of GO/PVA nanocomposites in time scales of up to 10^6—10^7 s. At 30 MPa stress level,
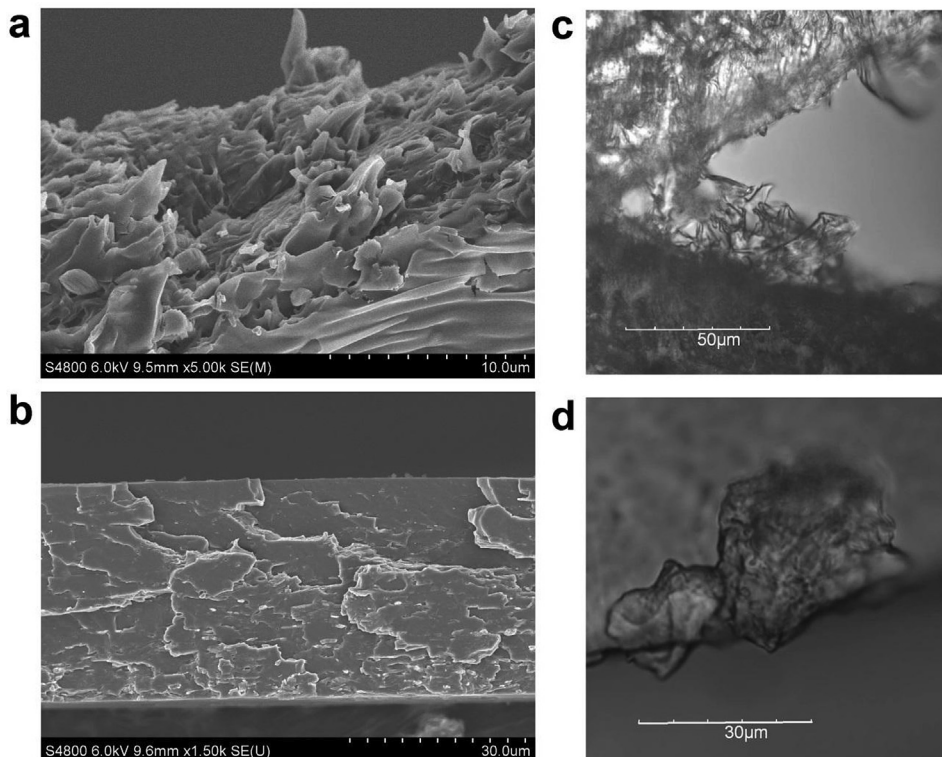

Fig. 8. SEM images of fracture surface of *s*-GO (a) and *l*-GO (b) based GO/PVA nanocomposites; confocal laser scanning microscopy images of *s*-GO (c) and *l*-GO based (d) GO/PVAGO/PVA nanocomposites perpendicular to the fracture surface.

l-GO platelets have better creep resistance than *s*-GO platelets inside the polymer matrix, implying better load-bearing capability in *l*-GO/PVA nanocomposites. However, with increased applied stress level up to 40 MPa, *l*-GO/PVA nanocomposites exhibit better creep resistance than *s*-GO/PVA nanocomposites within an earlier time range. The creep compliance of *l*-GO/PVA nanocomposites rapidly increases and becomes even larger than that of *s*-GO/PVA nanocomposites. We attribute the abruptly decreased creep resistance of *l*-GO/PVA nanocomposites to the presence of the folded and crumpled morphologies of *l*-GO sheets. Interfacial debonding easily occurs at a large applied stress level and long loading time, which then leads to local stress concentration as supported by the results in Fig. 5.Eventually, severe slippage of PVA chain segments occurs and increases creep compliance. Notably, this unexpected mechanical behavior of embedded *l*-GO sheets inside the polymer matrix has not been given attention in literature.

Fig. 8a shows the fracture surfaces of GO/PVA nanocomposites characterized by SEM. The fracture surface of *s*-GO/PVA nanocomposites is relatively rough and has layered microstructures. Obviously, the thickness of layered microstructures in *s*-GO/PVA nanocomposites is much larger than that of a single GO sheet we previously measured (~1 nm). The confocal laser scanning microscopy image taken perpendicularly to fracture surface of the *s*-GO/PVA nanocomposite (Fig. 8c) also shows a similar rough crack path. We attribute these microstructure features to protruded polymer-coated GO sheets [64], indicating strong H-bonding between GO and PVA. Unlike the rough fracture surface observed for the *s*-GO/PVA nanocomposites, the *l*-GO/PVA nanocomposites have a relatively smooth fracture surface (Fig. 8b). The confocal laser scanning image of *l*-GO/PVA nanocomposites in Fig. 8d reveals the apparent pulling out of folded and crumpled GO sheets from the matrix, indicating that local stress concentration induces brittle fracture. Such different fracture modes of GO/PVA nanocomposites agree well with the results of tensile, creep, and in situ micro-Raman analysis.

4. Conclusion

We prepared GO-based PVA composites with low filler contents up to 1 wt.% by solution-casting method. Two types of GO sheets with aspect ratios of ~1.5×10^3 and ~7.4×10^4 were utilized as reinforcing nanofillers. The tensile mechanical properties of GO/PVA nanocomposites obviously improve with increased filler content. Compared with *s*-GO/PVA nanocomposites, *l*-GO/PVA nanocomposites exhibit better mechanical performance because of their large aspect ratio. However, the increased trend of Young's modulus becomes negligible with further increasing GO content. Further characterization based on confocal laser scanning microscopy indicates that embedded *l*-GO sheets have folded and crumpled microstructures inside the matrix. Through in situ tensile—Raman spectroscopy, we have successfully monitored the stress-transfer process of GO sheets at the microscopic level and found that local interfacial debonding easily occurs for *l*-GO/PVA nanocomposites at relative large strain levels. This finding is further supported by MD simulation. Long-term creep tests confirm that interfacial debonding induces the increase in creep compliance of *l*-GO/PVA nanocomposites at high applied stress levels. These results can help elucidate mechanical reinforcement and deformation mode in 2D nanofiller based nanocomposites.

Appendix A. Supplementary data

Supplementary data related to this article can be found at http://dx.doi.org/10.1016/j.polymer.2015.05.003.

References

[1] Hull D, Clyne T. An introduction to composite materials. Cambridge University Press; 1996.

[2] Liu L, Barber AH, Nuriel S, Wagner HD. Mechanical properties of functionalized single-walled carbon-nanotube/poly (vinyl alcohol) nanocomposites. Adv Funct Mater 2005;15:975—80.

[3] Liu L, Tasis D, Prato M, Wagner HD. Tensile mechanics of electrospun multi-walled nanotube/poly (methyl methacrylate) nanofibers. Adv Mater 2007;19: 1228—33.

[4] Ma W, Liu L, Zhang Z, Yang R, Liu G, Zhang T, et al. High-strength composite fibers: realizing true potential of carbon nanotubes in polymer matrix through continuous reticulate architecture and molecular level couplings. Nano Lett 2009;9:2855—61.

[5] Tang L, Zhang H, Han J, Wu X, Zhang Z. Fracture mechanisms of epoxy filled with ozone functionalized multi-wall carbon nanotubes. Compos Sci Technol 2011;72:7—13.

[6] Dai Z, Gao Y, Liu L, Pötschke P, Yang J, Zhang Z. Creep-resistant behavior of MWCNT-polycarbonate melt spun nanocomposite fibers at elevated temperature. Polymer 2013;54:3723—9.

[7] Lee C, Wei X, Kysar JW, Hone J. Measurement of the elastic properties and intrinsic strength of monolayer graphene. Science 2008;321:385—8.

[8] Balandin AA, Ghosh S, Bao W, Calizo I, Teweldebrhan D, Miao F, et al. Superior thermal conductivity of single-layer graphene. Nano Lett 2008;8:902—7.

[9] Zhang Y, Tan YW, Stormer HL, Kim P. Experimental observation of the quantum hall effect and Berry's phase in graphene. Nature 2005;438:201—4.

[10] Potts JR, Dreyer DR, Bielawski CW, Ruoff RS. Graphene-based polymer nanocomposites. Polymer 2011;52:5—25.

[11] Kim H, Abdala AA, Macosko CW. Graphene/polymer nanocomposites. Macromolecules 2010;43:6515—30.

[12] Young RJ, Kinloch IA, Gong L, Novoselov KS. The mechanics of graphene nanocomposites: a review. Compos Sci Technol 2012;72:1459—76.

[13] Liu H, Brinson LC. Reinforcing efficiency of nanoparticles: a simple comparison for polymer nanocomposites. Compos Sci Technol 2008;68:1502—12.

[14] Rafiee MA, Rafiee J, Wang Z, Song H, Yu Z-Z, Koratkar N. Enhanced mechanical properties of nanocomposites at low graphene content. ACS Nano 2009;3: 3884—90.

[15] Steurer P, Wissert R, Thomann R, Mülhaupt R. Functionalized graphenes and thermoplastic nanocomposites based upon expanded graphite oxide. Macromol Rapid Comm 2009;30:316—27.

[16] Xu Z, Gao C. Situ polymerization approach to graphene-reinforced Nylon-6 composites. Macromolecules 2010;43:6716—23.

[17] Yang H, Li F, Shan C, Han D, Zhang Q, Niu L, et al. Covalent functionalization of chemically converted graphene sheets via silane and its reinforcement. J Mater Chem 2009;19:4632.

[18] Stankovich S, Dikin DA, Piner RD, Kohlhaas KA, Kleinhammes A, Jia Y, et al. Synthesis of graphene-based nanosheets via chemical reduction of exfoliated graphite oxide. Carbon 2007;45:1558—65.

[19] Schniepp HC, Li JL, McAllister MJ, Sai H, Herrera-Alonso M, Adamson DH, et al. Functionalized single graphene sheets derived from splitting graphite oxide. J Phys Chem B 2006;110:8535—9.

[20] Dreyer DR, Park S, Bielawski CW, Ruoff RS. The chemistry of graphene oxide. Chem Soc Rev 2010;39:228—40.

[21] She X, He C, Peng Z, Kong L. Molecular-level dispersion of graphene into epoxidized natural rubber: morphology, interfacial interaction and mechanical reinforcement. Polymer 2014;55:6803—10.

[22] Fu Y, Liu L, Zhang J, Hiscox WC. Functionalized graphenes with polymer toughner as novel interface modifier for property-tailored polyactic acid/ graphene nanocomposites. Polymer 2014;55:6381—9.

[23] Zhang Y, Mark JE, Zhu Y, Ruoff RS, Schaefer DW. Mechanical properties of polybutadiene reinforced with octadecylamine modified graphene oxide. Polymer 2014;55:5389—95.

[24] Bindu STK, Nair AB, Abraham BT, Sabura Beegum PM, Thacil ET. Microwave exfoliated reduced graphene oxide epoxy nanocomposites for high performance applications. Polymer 2014;55:3614—27.

[25] Zhang WD, Shen L, Phang IY, Liu T. Carbon nanotubes reinforced Nylon-6 composite prepared by simple melt-compounding. Macromolecules 2004;37:256—9.

[26] Liang J, Huang Y, Zhang L, Wang Y, Ma Y, Guo T, et al. Molecular-level dispersion of graphene into poly (vinyl alcohol) and effective reinforcement of their nanocomposites. Adv Funct Mater 2009;19:2297—302.

[27] Xu Y, Hong W, Bai H, Li C, Shi G. Strong and ductile poly (vinyl alcohol)/ graphene oxide composite films with a layered structure. Carbon 2009;47: 3538—43.

[28] Zhao X, Zhang Q, Chen D, Lu P. Enhanced mechanical properties of graphene-based poly(vinyl alcohol) composites. Macromolecules 2010;43:2357–63.

[29] May P, Khan U, O'Neill A, Coleman JN. Approaching the theoretical limit for reinforcing polymers with graphene. J Mater Chem 2012;22:1278–82.

[30] Bortz DR, Heras EG, Martin-Gullon I. Impressive fatigue life and fracture toughness improvements in graphene oxide/epoxy composites. Macromolecules 2012;45:238–45.

[31] Zandiatashbar A, Picu CR, Koratkar N. Control of epoxy creep using graphene. Small 2012;8:1676–82.

[32] Meyer JC, Geim AK, Katsnelson M, Novoselov K, Booth T, Roth S. The structure of suspended graphene sheets. Nature 2007;446:60–3.

[33] Fasolino A, Los J, Katsnelson MI. Intrinsic ripples in graphene. Nat Mater 2007;6:858–61.

[34] Liu TH, Gajewski G, Pao CW, Chang CC. Structure, energy, and structural transformations of graphene grain boundaries from atomistic simulations. Carbon 2011;49:2306–17.

[35] Zheng Q, Geng Y, Wang S, Li Z, Kim JK. Effects of functional groups on the mechanical and wrinkling properties of graphene sheets. Carbon 2010;48:4315–22.

[36] Chen S, Li Q, Zhang Q, Qu Y, Ji H, Ruoff RS, et al. Thermal conductivity measurements of suspended graphene with and without wrinkles by micro-Raman mapping. Nanotechnology 2012;23:365701.

[37] Zhu W, Low T, Perebeinos V, Bol AA, Zhu Y, Yan H, et al. Structure and electronic transport in graphene wrinkles. Nano Lett 2012;12:3431–6.

[38] Zang J, Ryu S, Pugno N, Wang Q, Tu Q, Buehler MJ, et al. Multifunctionality and control of the crumpling and unfolding of large-area graphene. Nat Mater 2013;12:321–5.

[39] Kim H, Macosko CW. Processing-property relationships of polycarbonate/graphene composites. Polymer 2009;50:3797–809.

[40] Wakabayashi K, Pierre C, Dikin DA, Ruoff RS, Ramanathan T, Brinson LC, et al. Polymer-graphite nanocomposites: effective dispersion and major property enhancement via solid-state shear pulverization. Macromolecules 2008;41:1905–8.

[41] Xu J, Wang K, Zu SZ, Han BH, Wei Z. Hierarchical nanocomposites of polyaniline nanowire arrays on graphene oxide sheets with synergistic effect for energy storage. ACS Nano 2010;4:5019–26.

[42] Zhao J, Pei S, Ren W, Gao L, Cheng HM. Efficient preparation of large-area graphene oxide sheets for transparent conductive films. ACS Nano 2010;4:5245–52.

[43] Potts JR, Shankar O, Du L, Ruoff RS. Processing–morphology–property relationships and composite theory analysis of reduced graphene oxide/natural rubber nanocomposites. Macromolecules 2012;45:6045–55.

[44] Gómez-Navarro C, Burghard M, Kern K. Elastic properties of chemically derived single graphene sheets. Nano Lett 2008;8:2045–9.

[45] Stankovich S, Dikin DA, Dommett GH, Kohlhaas KM, Zimney EJ, Stach EA, et al. Graphene-based composite materials. Nature 2006;442:282–6.

[46] Plimpton S. Fast parallel algorithms for short-range molecular dynamics. J Comput Phys 1995;117:1–19.

[47] Stuart SJ, Tutein AB, Harrison JA. A reactive potential for hydrocarbons with intermolecular interactions. J Chem Phys 2000;112:6472–86.

[48] Belytschko T, Xiao SP, Schatz GC, Ruoff RS. Atomistic simulations of nanotube fracture. Phys Rev B 2002;69:235430.

[49] Neek-Amal M, Peeters FM. Strain-engineered graphene through a nano-structured substrate. I Deform Phys Rev B 2012;85:195445.

[50] Affdl J, Kardos J. The Halpi-Tsai equations: a review. Polym Eng Sci 1976;16:344–52.

[51] Weibull W. Wide applicability. J Appl Mech 1951;18:293–7.

[52] Kim J, Kim F, Huang J. Seeing graphene-based sheets. Mater Today 2010;13:28–38.

[53] Tang Z, Kang H, Shen Z, Guo B, Zhang L, Jia D. Grafting of polyester onto graphene for electrically and thermally conductive composites. Macromolecules 2012;45:3444–51.

[54] Park O-K, Hwang J-Y, Goh M, Lee JH, Ku B-C, You N-H. Mechanically Strong and multifunctional polyimide nanocomposites using amimophenyl functionalized graphene nanosheets. Macromolecules 2013;46:3505–11.

[55] Potts JR, Murali S, Zhu Y, Zhao X, Ruoff RS. Microwave-exfoliated graphite oxide/polycarbonate composites. Macromolecules 2011;44:6488–95.

[56] Liu L, Gao Y, Liu Q, Kuang J, Zhou D, Ju S, et al. High mechanical performance of layered graphene oxide/poly (vinyl alcohol) nanocomposite films. Small 2013;9:2466–72.

[57] Gao Y, Liu L, Zu SZ, Peng K, Zhou D, Han BH, et al. The effect of interlayer adhesion on the mechanical behaviors of macroscopic graphene oxide papers. ACS Nano 2011;5:2134–41.

[58] Mohiuddin T, Lombardo A, Nair R, Bonetti A, Savini G, Jalil R, et al. Uniaxial strain in graphene by raman spectroscopy: g peak splitting, Grüneisen parameters, and sample orientation. Phys Rev B 2009;79:205433.

[59] Gong L, Kinloch IA, Young RJ, Riaz I, Jalil R, Novoselov KS. Interfacial stress transfer in a graphene monolayer nanocomposite. Adv Mater 2010;22:2694–7.

[60] Izer A, Bárány T. Effect of consolidation on the flexural creep behaviour of all-polypropylene composite. Express Polym Lett 2010;4:210–6.

[61] Jia Y, Peng K, Gong X-L, Zhang Z. Creep and recovery of polypropylene/carbon nanotube composites. Inter J Plast 2011;27:1239–51.

[62] Hine P, Ward I, Jordan N, Olley R, Bassett D. The hot compaction behaviour of woven oriented polypropylene fibres and tapes. I. Mechanical properties. Polymer 2003;44:1117–31.

[63] Dutta NK, Edward GH. Generic relaxation S spectra of solid polymers. I. Development of spectral distribution model and its application to stress relaxation of polypropylene. J Appl Polym Sci 1997;66:1101–15.

[64] Li Y, Yang T, Yu T, Zheng L, Liao K. Synergistic effect of hybrid carbon Nanotube–Ggraphene oxide as a nanofiller in enhancing the mechanical properties of PVA C composites. J Mater Chem 2011;21:10844–51.